Zhou, Y., Lühr, H., Alken, P. (2018): The Sidebands of the Equatorial Electrojet: General Characteristic of the Westward Currents, as Deduced From CHAMP. - *Journal of Geophysical Research*, *123*, 2, pp. 1457—1476.

DOI: http://doi.org/10.1002/2017JA024687

AGU PUBLICATIONS

JGR

Journal of Geophysical Research: Space Physics

RESEARCH ARTICLE
10.1002/2017JA024687

Key Points:
- A comprehensive characterization is given of the reverse current equatorial electrojet (EEJ) sidebands based on satellite data
- Average global features and main dependences on local time, season, and solar activity of the EEJ sidebands based on 5 years of CHAMP observations are presented
- A tidal analysis of relevant EEJ sideband parameters indicates the variability of the winds causing the sidebands

Correspondence to:
Y.-L. Zhou,
zhouyl@whu.edu.cn

Citation:
Zhou, Y.-L., Lühr, H., & Alken, P. (2018). The sidebands of the equatorial electrojet: General characteristic of the westward currents, as deduced from CHAMP. *Journal of Geophysical Research: Space Physics*, *123*, 1457–1476. https://doi.org/10.1002/2017JA024687

Received 17 AUG 2017
Accepted 19 JAN 2018
Accepted article online 29 JAN 2018
Published online 10 FEB 2018

The Sidebands of the Equatorial Electrojet: General Characteristic of the Westward Currents, as Deduced From CHAMP

Yun-Liang Zhou[1], Hermann Lühr[2], and Patrick Alken[3]

[1]Department of Space Physics, School of Electronic Information, Wuhan University, Wuhan, China, [2]GFZ German Research Centre for Geosciences, Potsdam, Germany, [3]Cooperative Institute for Research in Environmental Sciences, University of Colorado Boulder, Boulder, CO, USA

Abstract Based on 5 years (2001–2005) of magnetic field measurements made by the CHAMP satellite, latitudinal profiles of the equatorial electrojet (EEJ) have been derived. This study provides a comprehensive characterization of the reverse current EEJ sidebands. These westward currents peak at ±5° quasi-dipole latitude with typical amplitudes of 35% of the main EEJ. The diurnal amplitude variation is quite comparable with that of the EEJ. Similarly to the EEJ, the intensity is increasing with solar EUV flux, but with a steeper slope, indicating that not only the conductivity plays a role. For the longitude distribution we find, in general, larger amplitudes in the Western than in the Eastern Hemisphere. It is presently a common understanding that the reverse current EEJ sidebands are generated by eastward zonal winds at altitudes above about 120 km. In particular, a positive vertical gradient of wind speed generates westward currents at magnetic latitudes outside of 2° dip latitude. Interesting information about these features can be deduced from the sidebands' tidal characteristics. The longitudinal variation of the amplitude is dominated by a wave-1 pattern, which can primarily be attributed to the tidal components SPW1 and SW3. In case of the hemispheric amplitude differences these same two wave-1 components dominate. The ratio between sideband amplitude and main EEJ is largely controlled by the tidal features of the EEJ. The longitudinal patterns of the latitude, where the sidebands peak, resemble to some extent those of the amplitude. Current densities become larger when the peaks move closer to the magnetic equator.

Plain Language Summary Based on 5 years of magnetic field measurements by the CHAMP satellite, latitudinal profiles of the equatorial electrojet (EEJ) have been derived. This study provides a comprehensive characterization of the reverse current equatorial electrojet (EEJ) sidebands. The average global features and main dependences on local time, season, and solar activity of the EEJ sidebands are presented. A tidal analysis of relevant EEJ sideband parameters indicates the variability of the winds causing the sidebands.

1. Introduction

Due to the horizontal geomagnetic field geometry and the anisotropic conductivity of the stratified ionosphere, many peculiar phenomena arise in the equatorial ionosphere. One such phenomenon is the equatorial electrojet (EEJ), which is a relatively strong electric current in the *E* region ionosphere flowing along the magnetic equator at daytime. This narrow ribbon of enhanced ionospheric currents is primarily driven by the large-scale zonal polarization electric field in combination with the Cowling conductivity (Cowling, 1933). This enhanced conductivity builds up at the equator under the combined effects of a horizontal magnetic field and low-conductivity layers above and below the *E* region (e.g., Forbes, 1981).

By utilizing magnetic field observations from ground stations, sounding rockets, and low-Earth orbiting (LEO) satellites, numerous studies have been performed in the past several decades on the characteristics of the EEJ and related physical mechanisms (e.g., Agu & Onwumechili, 1981; Alken & Maus, 2007; Chapman, 1951; Egedal, 1947; Forbes, 1981; Ivers et al., 2003; Jadhav et al., 2002; Langel et al., 1993; Lühr & Manoj, 2013; Lühr et al., 2004; Onwumechili, 1997; Zhou et al., 2016). In these studies the authors have mainly paid attention to the eastward currents at the magnetic equator, namely, the main current of the EEJ.

Besides this main feature of the EEJ, frequently reverse magnetic field deflections are observed on the flanks of the ribbon, primarily in recordings from satellites (e.g., Cain & Sweeney, 1973; Lühr et al., 2004;

Onwumechili,1992; Onwumechili & Agu, 1980). For distinguishing them from the main EEJ at the magnetic equator, we term the related currents on the north and south sides "reverse current EEJ sidebands."

The mention of the EEJ sidebands in observations can be traced back to the 1970s. By using the POGO satellite total magnetic field observations, Cain and Sweeney (1972) had studied the signatures of the EEJ. They found the existence of high "shoulders" on the flanks off the magnetic equator in the latitudinal profiles of the magnetic EEJ signature (see their Figure 11). With respect to these shoulders, they stated that they seem to imply a frequent occurrence of westward currents at the flanks. Uncertainties in baseline level, however, prevented them from firm conclusions. Based on ground observations from Central Africa, Fambitakoye and Mayaud (1976) mentioned the frequent occurrence in the afternoon of a secondary reversed current ribbon, approximately twice as wide as the main ribbon. From nine ground stations in northeastern Brazil Hesse (1982) found clear depressions in the horizontal magnetic field profiles some degrees off the magnetic equator. This feature was interpreted as westward currents on the two flanks of the EEJ. All the interpretations from ground-based observations, however, were plagued by the uncertainty of a proper reduction of the solar quiet (Sq) background variation. By utilizing high-resolution magnetic field measurements of the CHAMP satellite, Lühr et al. (2004) were able to separate quite reliably the contributions between the Sq system and the EEJ. Subsequently, they calculated latitudinal profiles of the EEJ height-integrated current density through inversion of a dense series of line currents at *E* region altitude. They confirmed that reverse current signatures on the north and south sides of the main EEJ are a rather common feature of the EEJ at noontime. The sidebands of EEJ peak at latitudes about 5° away from the magnetic equator and exhibit a distinct variation with longitude. It was also shown that the peak amplitude of the sidebands amounts to about one third of the main EEJ current density at noontime. Later, the existence of westward current components at the flanks was also confirmed by interpreting the vector field magnetic signatures at CHAMP altitude. The large amplitude of the vertical *Bz* component variation with respect to the horizontal *Bx* deflection could only be explained by the effect of reverse current sidebands (Lühr & Maus, 2006). It has to be noted here that the reverse currents do not represent actual westward currents, as is obvious from Figure 2 in Lühr et al. (2004). The EEJ signature we are talking about is superimposed on the Sq system, and thus, a net zonal current is generally flowing eastward at low latitudes. Recently, Thomas et al. (2017) obtained the EEJ parameters from 1.5 years of Swarm magnetic field data. They derived latitudinal current density profiles by applying an empirical model to the magnetic field data. Besides the typical characteristics of the EEJ, the presence of the westward currents is shown peaking about 5° away from the magnetic equator. Their results indicated that the ratio of the total eastward flowing EEJ to westward return currents varies between 0.1 and 1.0. There appear certain hemispheric differences in the westward current bands on the two sides.

A sensible explanation for the occurrence of reverse current sidebands was provided by Richmond (1973). With the help of his EEJ model, he showed that height-varying eastward winds affect currents a few degrees off the magnetic equator more strongly than the currents at the magnetic equator. Based on in situ wind measurements above the EEJ in India and applying the approach outlined by Richmond (1973), Anandarao and Raghavarao (1979, 1987) found that vertical shear of zonal wind creates sidebands peaking at ±5° magnetic latitude and compresses the width of the main EEJ current band. More recently, Maus et al. (2007) and Alken et al. (2008) investigated the effects of the zonal wind distribution, as represented by the models HWM93 and HWM07, on *E* region current profiles at low latitudes. By varying the zonal wind vertical profile, to best fit the observed EEJ signature, they found that a positive vertical gradient (increasing eastward velocity with altitude) in the *E* layer causes EEJ sidebands peaking at ±5° magnetic latitude, which are in good agreement with current profiles deduced from CHAMP (e.g., Lühr et al., 2004).

In spite of the numerous studies, the general characteristics of the EEJ sidebands are not well known. There are a number of open issues. What are the dependences of the sidebands on local time and season? How do they vary with longitude and latitude? Is there a relation between the reverse current amplitude and the EEJ intensity?

We believe that the high-resolution magnetic field measurements made by CHAMP, which was in orbit for 10 years, can help to answer these questions. In this study we will first derive latitudinal profiles of the EEJ current density by inverting the magnetic field recordings from each equator pass of CHAMP. The amplitude and location of the EEJ sidebands can be determined from these profiles. For obtaining the general

properties of the EEJ sidebands, we statistically analyzed the variations with local time, latitude, longitude, solar activity, and hemisphere.

In the subsequent section we first introduce the data set and the approach for deriving the latitudinal profiles of the EEJ. The observational results will be presented in section 3. Then we will discuss our findings in the context of previous studies with special emphasis on the *E* region winds that are regarded responsible for the reverse currents. The main findings are summarized in section 5.

2. Data Processing

2.1. CHAMP Mission and OVM Data

The CHAMP (CHAllenging Minisatellite Payload) is a German small satellite mission for geoscientific and atmospheric research and applications, which was launched on 15 July 2000 into a near-circular polar orbit (inclination: 87.3°) with an initial altitude of 456 km (Reigber et al., 2002). By the end of the mission, 19 September 2010, the orbit had decayed to 250 km. With the onboard magnetometers CHAMP has provided highly precise magnetic field measurements for about 10 years, allowing to investigate the spatial and temporal variability of ionospheric currents.

For the present study we utilize the scalar magnetic field data, which are based primarily on the absolute scalar Overhauser Magnetometer (OVM) measurements. The OVM was developed and manufactured by LETI, Grenoble, France, and it sampled the ambient field strength at a rate of 1 Hz with an absolute accuracy of $<$0.5 nT. In this study the fully calibrated Level-3 magnetic field products (product identifier: CH-ME-3-MAG) are used.

2.2. Derivation of EEJ Profiles From Magnetic Data

The EEJ profiles are derived from the scalar magnetic field readings. For isolating the magnetic field signature caused by the EEJ, a number of other contributions to the original recordings have to be removed. We first applied a correction of the diamagnetic effect caused by pressure gradients in the ambient plasma. A suitable formula for this correction is given by (Lühr et al., 2003)

$$\Delta B = nk(T_i + T_e)\frac{\mu_0}{B} \tag{1}$$

where n is the electron number density, k is the Boltzmann constant, T_i and T_e are the ion and electron temperatures, respectively, μ_0 is the susceptibility of free space, and B is the ambient magnetic field strength. Quantities that go into equation (1), such as electron density and temperature and total magnetic field, are taken directly from CHAMP measurements. For the ion temperature (in units K) we use an estimate, as suggested by the model of Köhnlein (1986), $T_i = 900 + 100\cos\left[\frac{\pi}{12}(\mathrm{MLT} - 13)\right]$, where MLT denotes the magnetic local time in hours. Since the plasma data are sampled at a lower rate, the diamagnetic effect is calculated every 15 s. With the help of a cubic spline we then obtain values for the diamagnetic effect synchronous with the magnetic field readings at a cadence of 1 s. A more detailed description of the diamagnetic effect features at low latitudes can be found in Lühr et al. (2003, 2004). For the study of the EEJ sidebands we regard the diamagnetic correction as relevant, because the electron density enhancements associated with the equatorial ionization anomaly can introduce systematic variations of the magnetic field near the magnetic equator in the vicinity of the sidebands.

In addition to the diamagnetic effect, the core, crustal, and magnetospheric fields have to be removed from the original magnetic data. CHAOS-6 (Finlay et al., 2016) was used to remove the core field to spherical harmonic degree 15. The crustal field contribution for spherical harmonic degrees 16 to 133 is removed using the MF7 model (Maus et al., 2008), and the external field part of POMME-6 (Lühr & Maus, 2010) is used to remove the magnetospheric fields. The sum of these contributions is subtracted from the CHAMP scalar data. Then, the contribution of midlatitude Sq currents, as well as unmodeled external fields, is filtered out on a track-by-track basis using internal and external spherical harmonic field parameterizations, resulting in a clean EEJ signal. More details about these external field contributions can be found in Alken et al. (2013). Finally, we inverted the obtained EEJ signal for the height-integrated sheet current density using a model of line currents, separated by 50 km in latitude and flowing along lines of constant quasi-dipole latitude at 110 km altitude in the low-latitude *E* region. Since the EEJ signal is weak during the night, we limit our

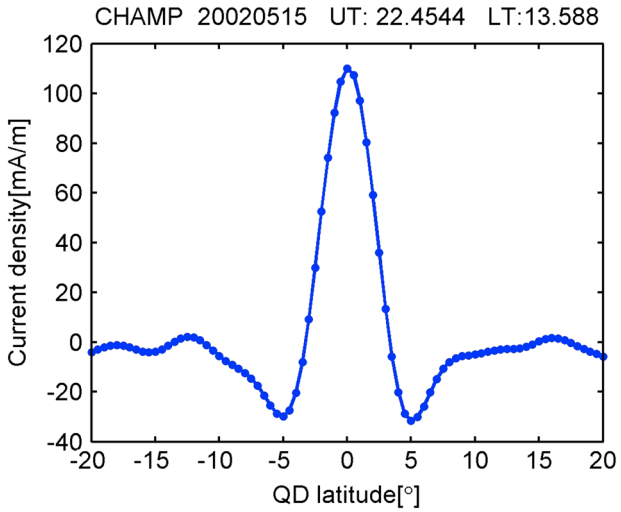

Figure 1. Example of an EEJ current profile derived by inverting CHAMP magnetic field measurements. Typical features are the peak in eastward current density at the magnetic equator and the westward current sidebands, peaking here 5° in latitude off the magnetic equator.

analysis to daytime crossings of the magnetic equator from 0600 to 1800 LT. As a result we obtain from each orbit a profile of height-integrated current density within the latitude range of ±20° quasi-dipole (QD) latitude (Richmond, 1995) at a resolution of 0.5°. More details about the EEJ current inversion can be found in Alken et al. (2013, 2015).

3. Observations

Here we first describe a typical EEJ current profile. From that the typical features of the current distribution can be deduced. In later parts the statistical properties of the sidebands and of the ratio between the EEJ main current and reverse currents are presented.

3.1. The EEJ Current Profile

Figure 1 presents an example of an EEJ current density latitudinal profile derived from CHAMP magnetic field measured on 15 May 2002. For this event the universal time (UT) and local time (LT) of CHAMP equator crossing were about 22:30 UT and 13.6 LT, respectively. Around this time quiet magnetic conditions prevailed ($Kp = 2$). This graph depicts general features of an EEJ latitudinal profile. A prominent characteristic is the collocation of the main current peak with the magnetic equator. The main current is flowing eastward, reaching a peak amplitude of about 110 mA/m. The width at half-peak amplitude amounts to 4° in latitude. Off the magnetic equator, exceeding 3° in latitude, the current reverses from eastward to westward. This part of the profile, beyond those latitudes, we call reverse current EEJ. It can be seen that the sidebands peak at ±5° QD latitude and the peak current densities in this case are −31.7 and −29.9 mA/m in the Northern and Southern Hemispheres, respectively. The ratio of the sideband peak current density to the main EEJ is about 28%. Beyond a QD latitude of 10° the derived current density oscillates slightly about zero. This is typically due to local *F* region currents flowing near the satellite or it could be an artifact of the regularization used to remove the Sq signal.

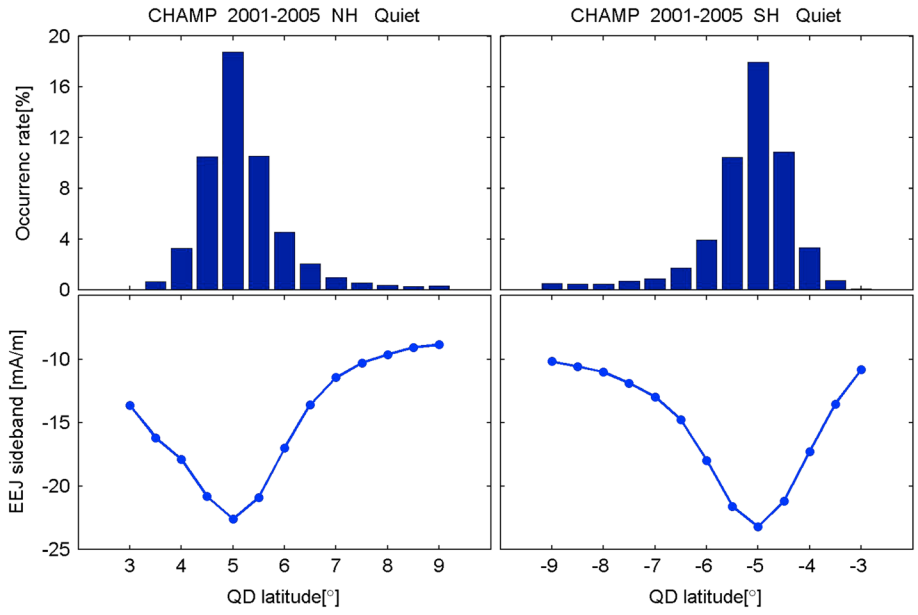

Figure 2. Latitudinal variation of the EEJ sidebands. Distribution (top) of the peak location occurrence rate and (bottom) of the peak current density.

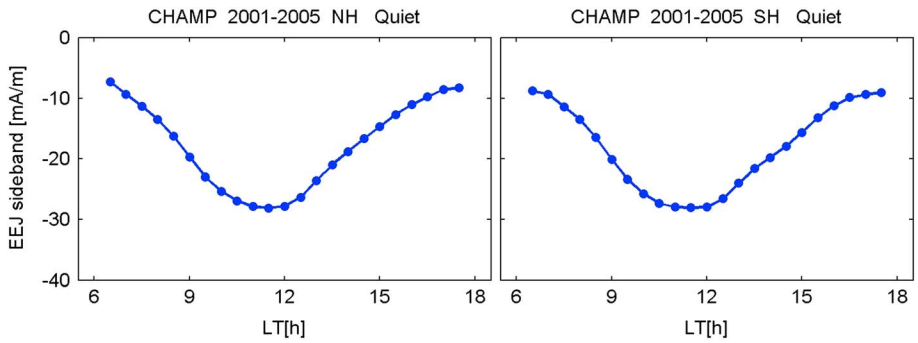

Figure 3. Diurnal variation of the EEJ sideband peak current density.

3.2. Statistical Characteristics of Reverse Currents in the Sidebands

Having seen the general characteristic of an EEJ current density profile, we now want to take a look at the statistical characteristics of these reverse current EEJ sidebands. For the statistical analysis we consider in this study the time period from 2001 to 2005, experiencing solar activity from high to moderate levels. Five years are just needed by CHAMP to obtain an even coverage of local times in all seasons. Within those years the satellite crossed the equator in total 27,604 times. We applied a rigorous selection procedure for avoiding false interpretations. From all low-latitude passes only the events with eastward EEJ current density exceeding 10 mA/m have been considered; in this way counterelectrojets are omitted. And the eastward current peak had to appear within ±1° QD latitude. Additionally, in order to limit the effects from geomagnetic disturbances, only data during quiet conditions ($Kp \leq 3$) were utilized. All this resulted in 20,178 quiet time passes. Second, we search for the minimum current densities in the Northern and Southern Hemispheres. For the sidebands to be considered we requested that the peaks in current density are located within 3° to 9° in latitude off the magnetic equator and the reverse current density has to exceed −6 mA/m. Considering all our selection criteria, 9,418 events with sidebands are available for the statistical investigation. This corresponds to an occurrence rate of 47%. For further analysis of the selected EEJ sidebands their peak current densities and their latitudes in both hemispheres are considered. We also make use of the ratios between the main EEJ current density peak and the values of the sideband peaks in the two hemispheres for studies presented in section 3.3.

Figure 2 shows the latitudinal distribution of the sideband current density peaks. The top panel provides the occurrence frequency of peak locations within bins of 0.5° in magnetic latitude, separately for the two hemispheres. For example, in the Northern Hemisphere the largest occurrence rate appears at 5° QD latitude with the value of 18.8%. This means that there are 3,793 events peaking at 5° QD latitude. The rate is down to about 10.5% at 4.5° and 5.5° QD latitude. Occurrence frequencies drop off quite steeply away from 5° QD latitude. For the Southern Hemisphere the latitude distribution of the sideband peak locations is similar to that in the Northern Hemisphere.

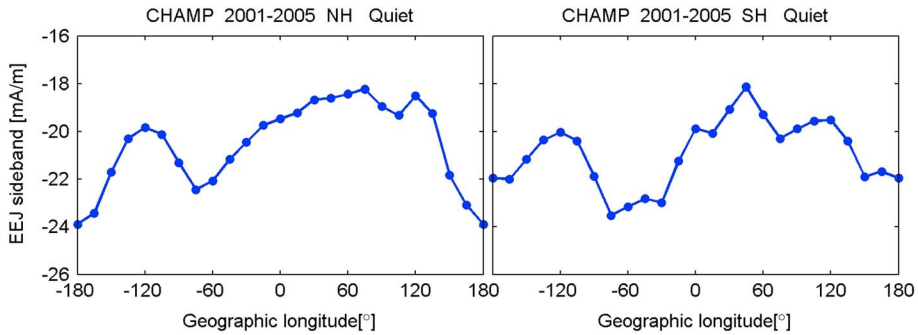

Figure 4. Longitudinal variation of the EEJ sideband peak current density.

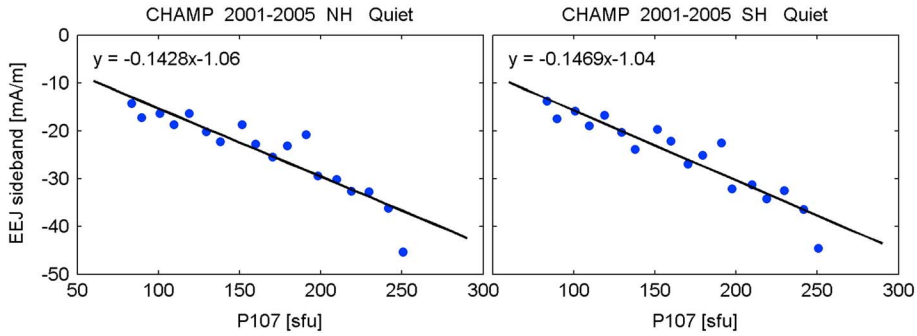

Figure 5. Dependence on the solar flux index, *P10.7*, of the EEJ sideband peak current density.

The bottom panel of Figure 2 shows the latitudinal distribution of the reverse current peak density. Here each blue dot denotes the median value of the peak current densities in each of the 0.5° wide latitude bins. The prominent feature in the panel is that largest peak current amplitudes appear at 5° QD latitude, collocated with the highest occurrence rate of sideband locations. The median values of the peak sideband current densities are −22.6 and −23.2 mA/m for the Northern and Southern Hemispheres, respectively. Away from the QD latitude of 5°, the amplitudes drop off rapidly.

Figure 3 shows the average local time variation of the sideband current densities for both hemispheres. The blue dots represent again median values of the peak amplitudes in the different LT bins. The sideband peak amplitudes exhibit a clear local time variation, showing similar dependences in both hemispheres. Largest amplitudes are found around 11.5 LT with mean current densities of about −28 mA/m. Toward morning and evening hours the peak amplitude of the sidebands becomes small. The curves in Figure 3 are quite similar to the diurnal variation of the EEJ intensity.

The average distribution of the sideband amplitude with longitude is presented in Figure 4. Here the blue dots represent the median values of the peak current density in the 15° wide longitude bins. It can be seen that the sideband peak amplitudes show two prominent maxima at about 60°W and 180°E in longitude for both hemispheres, although there are certain differences between the two hemispheres. Smallest current densities appear in the regions around 120°W and 60°E in longitude.

We have also checked the dependence of current density on solar EUV radiation. Figure 5 presents the response of the sideband peak amplitude to the radio flux index *P10.7*. Here *P10.7* is calculated as *P10.7 = (F10.7 + F10.7A)/2*, where *F10.7A* is the 81 days averaged value of *F10.7*. The median values of the sideband peak amplitudes for different levels of *P10.7* are represented by blue dots separately for both hemispheres. The high degree of correlation justifies the analysis of a linear regression between the sideband amplitude and *P10.7*. Numerical values for the regression line, which is added in black, are listed in the upper

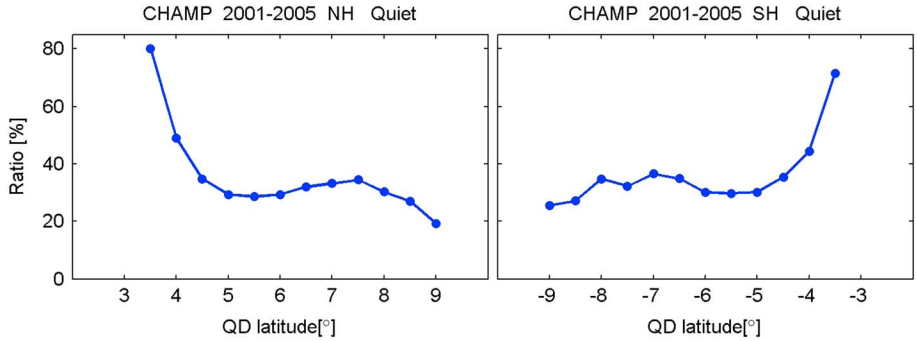

Figure 6. Latitudinal variation of the ratio between sideband and main EEJ current density.

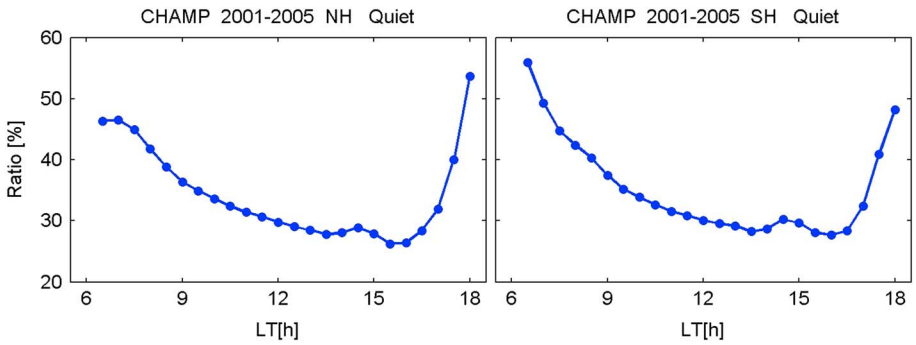

Figure 7. Local time variation of the ratio between sideband and main EEJ current density.

left corner. Here again the obtained slopes in the two hemispheres are quite similar. A rise of solar flux units by 70 causes a current density increases by 10 mA/m.

3.3. Statistical Properties of the Current Ratio

The current density of the EEJ sidebands is dependent on several quantities. These are primarily the zonal wind configuration and the conductivity. In order to better separate the effects, we have also investigated the statistical properties of the ratio between the sideband and the main EEJ peak current densities. The data set utilized here is the same as introduced in section 3.2.

Figure 6 presents the latitudinal distribution of the ratio. Different from the latitudinal distribution of the sideband amplitude (see Figure 2), the ratio between the peak currents stays at fairly constant level from 5° to 9° in QD latitude. On average the ratio varies over this latitude band around 29.2% (31.2%) in Northern (Southern) Hemisphere. For peak latitudes less than 5° the ratio sharply rises. This result suggests that the sidebands become more important when they occur closer to the equator.

Figure 7 depicts the average local time variation of the ratio. It is quite different from the local time variation of the sideband amplitudes, as shown in Figure 3. The ratio decreases almost monotonically from the morning hours to the early evening. Interestingly, we find that the ratio exhibits a small local maximum at 14.5 LT. The rapid increase toward sunset hours is probably due to the decaying EEJ intensity in that time sector. Although there are some differences in the morning and evening parts, the local time variations of the ratios in both hemispheres are similar from 9 to 17 LT.

The longitude variation of the ratio is shown in Figure 8. Different from the peak current densities of the sidebands, the ratios exhibit a rather small dependence on longitude. In these annual averages a wave number 4 pattern is clearly visible. The corresponding maxima appear at about 150°W, 45°W, 45°E, and 165°E in longitude. These locations of the ratio maxima correspond rather well to the longitudes of the troughs in EEJ

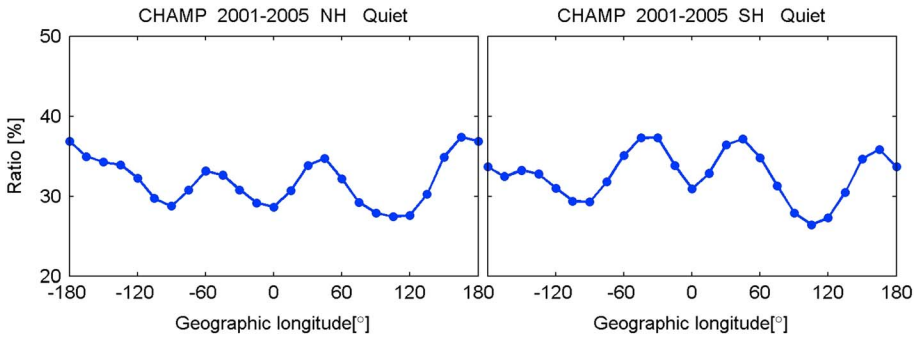

Figure 8. Longitude variation of the ratio between sideband and main EEJ current density.

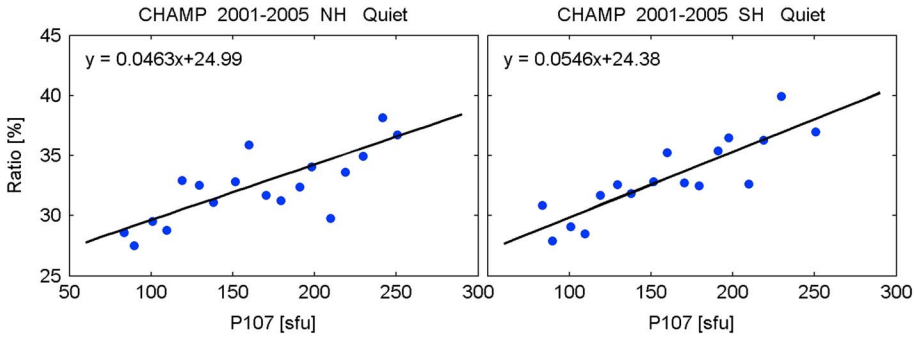

Figure 9. Solar flux dependence of the ratio between sideband and main EEJ current density.

amplitudes (e.g., Zhou et al., 2016). The longitudinal patterns of the ratio are obviously caused primarily by modulation of the mean EEJ intensity distribution.

We also analyzed the solar activity dependence of the ratio, which is presented in Figure 9. It can be seen that the ratio increases when the *P10.7* is growing. Compare with the *P10.7* dependence of the sideband peak amplitudes (Figure 5), the data points are more scattered; therefore, the difference in slopes obtained for the Northern and Southern Hemispheres is probably not significant. Obviously, the sideband amplitudes grow faster than the EEJ intensity with increasing solar flux.

4. Discussion

In this study we investigated latitudinal profiles of EEJ sheet current density, which are superimposed on the Sq currents. We have shown that these profiles exhibit frequently reverse current sidebands. These wind-driven modifications of the EEJ current distribution are known since the 1970s. But it has been difficult to characterize them in detail from their small ground magnetic effects, due to the cancelation of oppositely directed currents (see, e.g., Reddy & Devasia, 1981). As a consequence, the reverse current sidebands have been discussed quite controversially in the past (e.g., Hesse, 1982). Magnetic field measurements by LEO satellites on polar orbits have the advantage of homogeneous and closely spaced sampling along their orbit, and they are thus more suitable for deriving latitudinal profiles of the electrojet. Based on accurate CHAMP magnetic field measurements, it has been convincingly shown that reverse current EEJ sidebands actually exist (e.g., Lühr & Maus, 2006; Maus et al., 2007).

Since the pioneering work of Richmond (1973), it is known that zonal winds in the ionosphere have a significant influence on the structure of the EEJ. Within the dynamo layer winds drive currents in the same direction. Zonal winds occurring above about 120 km cause *E* layer currents in opposite direction. However, according to his equation (18), steady zonal winds within a fluxtube have little effect on current density. Making use of this formalism, for example, Fambitakoye et al. (1976) and later Anandarao and Raghavarao (1979) showed that a vertical shear of zonal wind near the equator just above the *E* layer is most efficient in modifying the EEJ current profile. A positive altitude gradient (e.g., increasing eastward velocity) in that altitude range causes westward currents on the flanks of the EEJ. In addition, it makes the main EEJ channel narrower in latitude. Making use of actual vertical wind profile measurements over India, Anandarao and Raghavarao (1979) could predict the existence of reverse currents at the flanks.

Maus et al. (2007) were the first to derive from the latitudinal current profiles of the EEJ information about the electric field and wind distribution in the equatorial region. When constraining the equatorial electric field, they could estimate vertical wind profiles. Alken et al. (2008) employed this approach later for checking the quality of the horizontal wind models HWM93 and HWM07. They clearly confirmed the preference of the more recent HWM07 zonal wind profiles at *E* region altitudes for reproducing the observed EEJ current profiles. In the examples they show, one can see that the wind shear above 115 km altitude is most important for the reverse currents peaking near 5° magnetic latitude. Fairly small gradients of about 5 m/s/km are sufficient to produce sidebands with −20 mA/m peak current density.

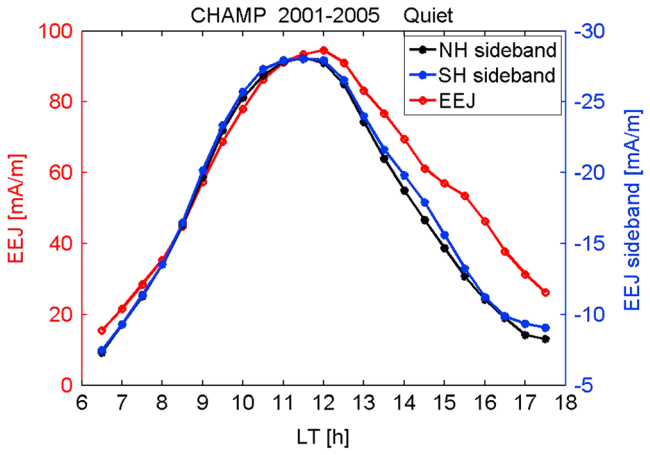

Figure 10. Mean local time variations of the main EEJ and the sidebands' current densities.

In a recent study Thomas et al. (2017) have deduced properties of the EEJ from 1.5 years of Swarm magnetic field data. They also report the presence of reverse current EEJ sidebands. However, they took a quite different approach for the estimation of current density profiles. In detail, they did not consider the diamagnetic effect, estimated the Sq contribution by fitting a degree 5 polynomial to the residual midlatitude magnetic field, and inverting the remaining low-latitude magnetic field by applying a predefined function for obtaining current density. Due to these clear differences in analysis, their results cannot directly be compared with the properties of the EEJ sidebands presented here. Their limited data set furthermore does not allow for a decoupling of seasonal/local time variations. Therefore, their longitudinal distributions of amplitude and latitude do probably not represent the true mean variations of these quantities.

4.1. Statistical Properties of Reverse Currents

The reverse current sidebands of the EEJ are a quite common phenomenon. In order to avoid false detections, we selected only events, which surpassed certain minimum current density peak values of the eastward EEJ and reverse currents; see section 3.2. Under these constraints sidebands are found in about 47% of all cases. On global average the appearance in the Northern and Southern Hemispheres is quite symmetric. However, when looking at the longitudinal distribution, as shown in Figure 4, we find regions of stronger and weaker current densities. Large current strengths are found in the Pacific sector around 180° longitude, in particular in the Northern Hemisphere, and in the South American, Atlantic region around 60°W, more pronounced in the Southern Hemisphere. In these two sectors stronger zonal wind shear seems to prevail. Besides the wind, also, the conductivity is expected to influence the reverse current strength. This is confirmed by the amplitude dependence of the sidebands on the solar flux index *P10.7* (Figure 5). There is definitely a longitudinal variation of the ionospheric conductivity that influences both the main EEJ and the sidebands. By considering the ratio between the peak current densities of the two systems, conductivity effects should cancel out. The annual average of the ratio, shown in Figure 8, exhibits a rather flat distribution over all longitudes. There appear three prominent peaks, over the Atlantic, Eastern Africa, and Central Pacific. These mark regions of stronger zonal wind shear or weaker EEJ. It is found that over Eastern Africa the amplitude of the main EEJ is particularly small during the years considered in this study.

We checked also the dependence of the ratio on the solar flux level (see Figure 9). The ratio is growing with increasing *P10.7*. Since conductivity effects should have canceled out in the ratio, the remaining increase suggests a stronger shear of the zonal wind for higher solar flux. This inference should probably be checked in future measurement campaigns.

Anandarao and Raghavarao (1987) had also modeled the influence of meridional wind, *v*, on the equatorial current distribution. Under the action of the Lorentz force, $v \times Br$ (here *Br* is the radial magnetic field component), a positive northward wind will generate a westward electric field in the Northern Hemisphere and an eastward electric field in the Southern Hemisphere, a few degrees off the magnetic equator. When considering the effect of meridional wind on our sidebands, we can expect an asymmetry between the hemispheres. From Figure 4 we deduced stronger westward currents over the northern part in the Central Pacific. This infers northward meridional winds. Conversely, the larger sidebands in the south over the Atlantic imply southward winds. One has to keep in mind, however, that these results are annual averages, which may vary from season to season.

When looking at the latitude distribution of current density (see Figure 2, bottom) sidebands peak on average 5° in latitude off the magnetic equator. But for a number of cases current peaks are observed at other latitudes (see Figure 2, top). Of interest may be the ratio between the peak current densities of the EEJ and the sidebands. The curves in Figure 6 imply that the relative amplitudes of the sidebands show only little dependence on latitude beyond 5° QD latitude. But ratios from peaks at lower latitudes progressively increase as appearing closer to the equator. These observations are consistent with the results of Reddy and Devasia (1981) who modeled the effects of various zonal wind profiles on the latitudinal distribution

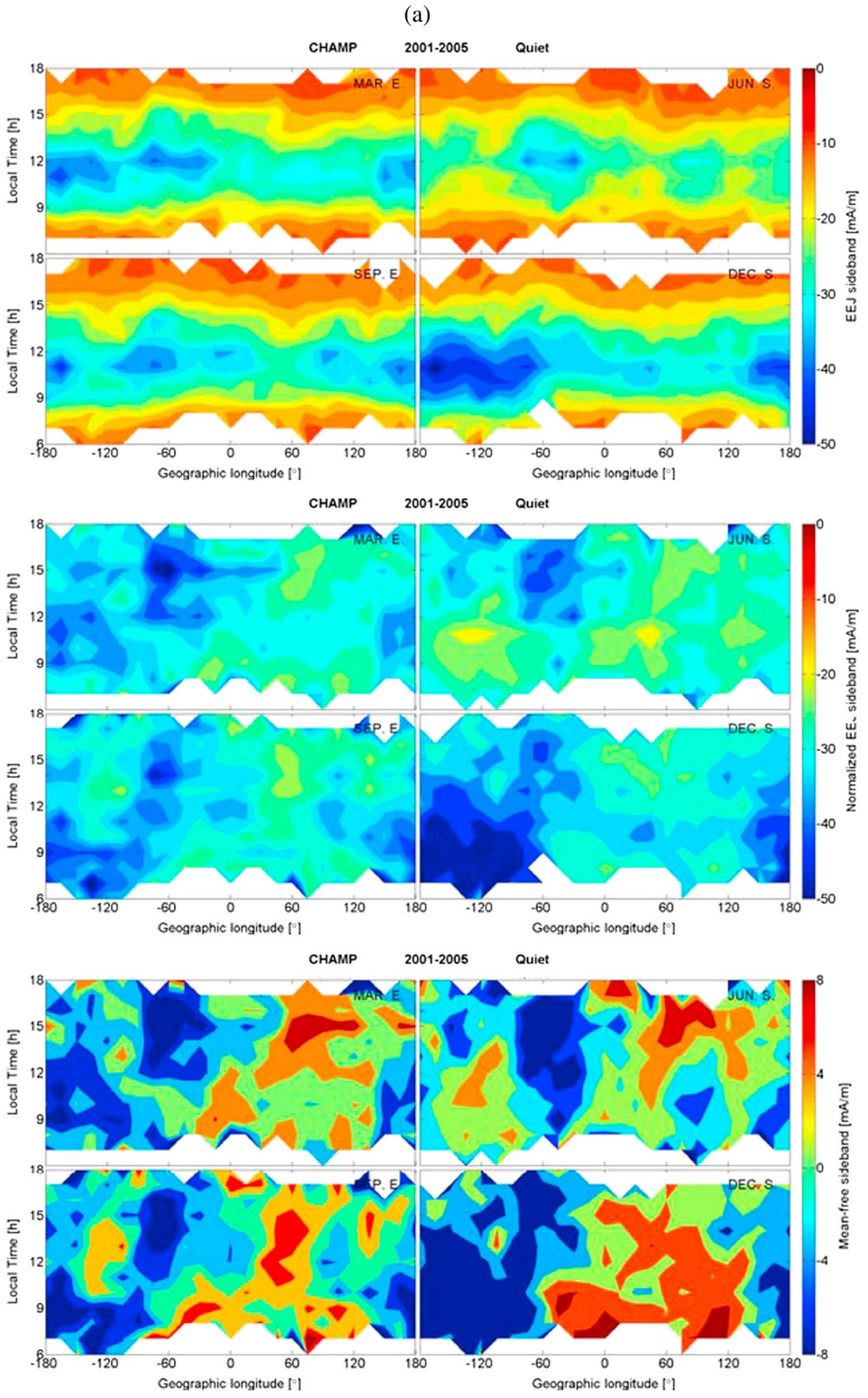

Figure 11. (a) Distribution of EEJ sideband current density in local time versus longitudinal frames, separately for the four seasons. The groups of panels from top to bottom show the original peak current amplitudes, the values normalized to the noon value, and the mean-free amplitude values after removal of longitudinal means. (b) Tidal analysis of the sideband peak current density. The top panels show the current density distribution as reconstructed from the tidal model. At the bottom the residuals between observation and model are shown.

(b)

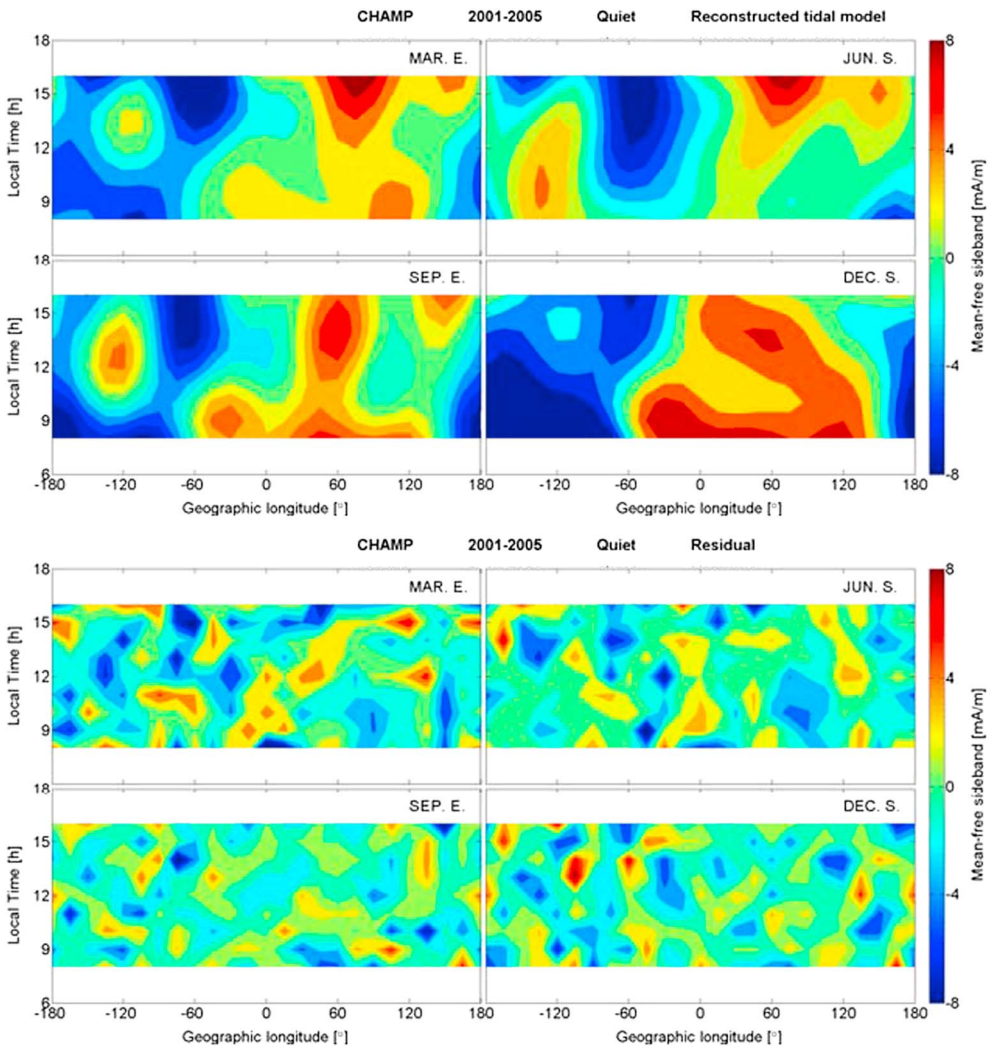

Figure 11. (continued)

of current density. In case of steeper vertical positive gradients of the wind velocity just above the *E* layer the reverse current sideband peaks appear closer to the equator and have larger amplitudes. At the same time the main electrojet gets weaker and the width narrower.

The local time variation of the sideband amplitude (see Figure 3) is rather similar to that of the electrojet attaining largest values around 11:30 LT. However, when looking at the ratio between the peak values (see Figure 7), differences become apparent. The ratio continuously decreases from the morning to the later afternoon hours. In order to find an explanation for this change in ratio, the local time variations of the main EEJ and the EEJ sideband current densities are shown as Figure 10. The curve of the northern hemisphere sideband almost perfectly tracks that of the main EEJ. When comparing the scales on both sides of the graph, we find a factor of 4 smaller range and a bias of 5 mA/m for the sidebands. This constant current density bias is the cause for the local time-dependent decrease of the ratio in Figure 7. In the Southern Hemisphere mean amplitudes are almost identical with those in the north before noon but somewhat larger thereafter. Presently, we cannot offer a conclusive explanation for the bias current density.

4.2. Seasonal and Local Time Variation of the EEJ Sidebands

So far, we have discussed the annual average characteristics of the reverse current sidebands. Earlier studies have identified thermospheric winds as an important driver for these reverse currents. Winds on the other

Table 1
Results of the Tidal Analysis (Amplitude and Phase) of the Reverse Current Peak Amplitudes

	NH and SH amplitude							
	Jun		Dec		Mar		Sep	
	Amp. (mA/m)	Phase (Hour)	Amp. (mA/m)	Phase (Hour)	Amp. (mA/m)	Phase (Hour)	Amp. (mA/m)	Phase (Hour)
DE3:	1.99	21.9	1.69	18.7	2.41	21.9	2.04	22.4
DE2:	1.52	9.9	1.20	12.3	1.14	12.3	1.08	12.2
TW1:	0.67	2.5	0.74	3.9	0.59	3.3	1.00	2.7
SW3:	4.37	6.3	5.38	10.2	2.90	7.3	3.17	9.2
SW4:	0.44	0.3	3.04	5.8	1.45	6.0	1.52	4.6
TW4:	2.15	4.0	3.48	7.0	1.61	3.7	1.70	7.4
SPW1:	2.59	76.0°	7.51	65.3°	4.72	67.5°	4.08	72.3°
SPW2:	2.41	52.6°	1.47	159.2°	0.47	59.5°	0.88	43.3°
SPW4:	1.12	0.4°	0.83	25.9°	1.93	89.5°	0.83	64.2°

Note. The values from the Northern and Southern Hemispheres have been combined. The phase represents the local time, at which the tidal maximum passes the Greenwich meridian. In case of stationary waves, SPW, the longitude of maximum is listed.

hand are strongly modified by solar tides. For that reason we investigated the tidal properties of the different sideband features. It is furthermore expected that the tidal characteristics vary with season. Subsequently, we thus present separate analysis for the four seasons.

Figure 11a shows the sideband amplitude distribution in local time versus longitude frames. This representation is well suited for depicting solar tidal structures. Please note that the warm colors indicate low amplitudes and blue large negative values. The diurnal variation is clearly visible in all panels of the top part. This is mainly reflecting the change in ionospheric conductivity. Since we are more interested in the characteristics of the zonal wind, we normalize the amplitudes at different local times to the noontime peak using the average LT shape of the curves in Figure 3. Results of that procedure are shown in the middle part of Figure 11a. Next, we remove the zonal averages hour by hour from the current densities. By this procedure the signature of migrating tides is removed, but the present data set is anyhow not suitable for deriving them because we have covered only daytime hours in our EEJ analysis. Still, from Figure 10 we can deduce a mean semidiurnal variation of about ±10 mA/m. This can be compared with the tidal amplitudes derived below.

The normalized and mean-free data set (bottom part) is the basis for tidal analysis. There is a rather clear separation between small amplitudes (reddish) in the Eastern Hemisphere and large (blue) in the Western Hemisphere. The wave-1 dominance is also reflected by the tidal analysis. Since we have only a limited number of local time hours available, we cannot apply a rigorous spectral analysis covering the full range of tidal components. Rather, we use the same approach as Zhou et al. (2016) and try to find the main tidal components. Our choice is validated by checking the residuals for systematic features. Obtained tidal amplitudes and phases are listed separately for the four seasons in Table 1. The synthesized longitudinal patterns of the sideband amplitudes, based on the derived tides, are shown at the top in Figure 11b. Prominent features are clearly visible here. The remaining residuals at the bottom show no systematic features, thus supporting our choice of tidal components.

The stationary SPW1 and the semidiurnal westward propagating SW3 (both contribute to wave-1) are the dominating tidal components in all seasons (see Table 1). The phase of SPW1 varies around 70° longitude, marking the amplitude minimum in the Indian sector. Large EEJ sidebands are expected correspondingly around −110° longitude in the West Pacific. The crest of SW3 migrates westward through all longitudes within 12 h of local time. Peak amplitudes from this tidal component cross the Greenwich meridian between 13 and 15 LT. A superposition of these two dominating tides occurs near −110° longitude around 06 and/or 18 LT. These hot spots are clearly visible in Figure 11b as dark blue patches, varying somewhat from season to season.

During the equinox seasons the tidal component DE3 is the third in line (see Table 1). This wave-4 pattern is known to be excited by deep convection in tropical regions of the troposphere in particular during equinoxes

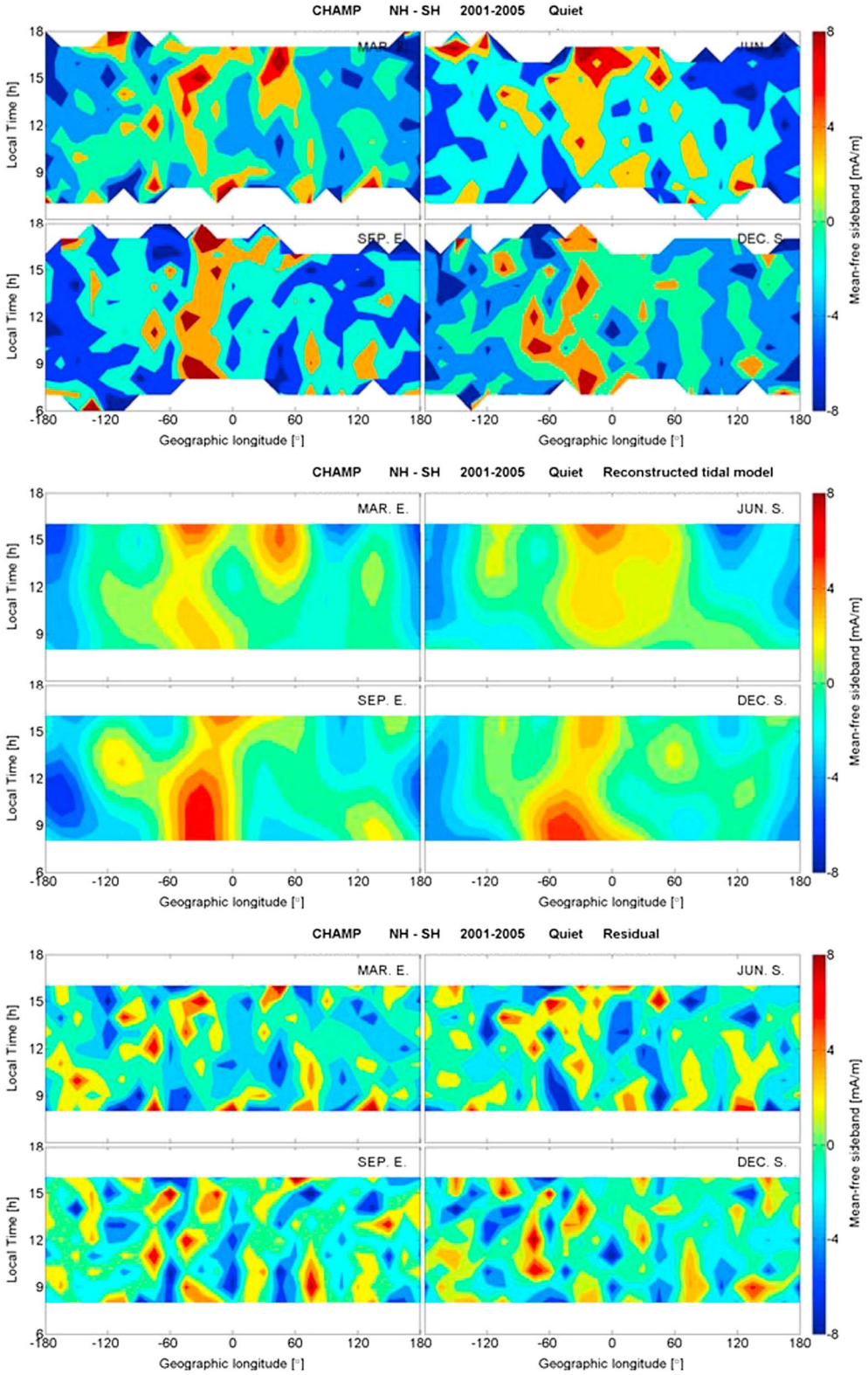

Figure 12. Tidal analysis of the difference between EEJ sideband current densities in the Northern and Southern Hemispheres. From top to bottom shown are the mean-free differences, the longitudinal patterns as reconstructed from the tidal model, and the residuals between observation and model.

Table 2
Same as Table 1 but for the Differences Between Northern and Southern Hemisphere Current Densities

	NH-SH amplitude							
	Jun		Dec		Mar		Sep	
	Amp. (mA/m)	Phase (Hour)	Amp. (mA/m)	Phase (Hour)	Amp. (mA/m)	Phase (Hour)	Amp. (mA/m)	Phase (Hour)
DE3:	1.06	0.1	1.55	22.9	1.30	5.2	0.65	21.5
DE2:	0.62	11.5	0.31	13.2	0.55	7.5	0.78	12.5
SW3:	2.37	1.7	1.57	9.0	1.50	2.6	0.85	4.8
SW4:	0.70	5.5	1.00	5.3	0.65	5.7	1.81	5.6
TW4:	1.74	1.4	1.51	6.5	1.36	1.0	1.49	2.9
SPW1:	2.08	333.8°	1.94	356.7°	2.04	332.0°	2.56	340.5°
SPW2:	0.49	14.3°	1.18	134.7°	0.56	125.3°	1.59	147.6°
SPW4:	0.88	77.2°	0.78	85.5°	1.88	59.0°	0.96	67.5°

(e.g., Hagan & Forbes, 2002). Oberheide et al. (2006) have earlier confirmed these tidal signatures in zonal winds of Thermosphere, Ionosphere, Mesosphere Energetics and Dynamics (TIMED) measurements. It is therefore no surprise that also the vertical gradient of the zonal wind is modified by that tide.

During December season the semidiurnal SW4 is also outstanding. Lühr and Manoj (2013) had earlier identified it as the dominant tidal component modulating the EEJ in that season. They report a wave phase of about 11 LT, which fits the time 5.8 LT of sideband minimum listed in Table 1. Generally, the tidal modulation of the sideband amplitudes is significantly larger around December than during other seasons. Presently, we have no conclusive explanation for it. Overall, the tidal features of the sideband amplitudes are quite similar to those of the EEJ.

In section 3 we have shown that the sidebands in the two hemispheres are quite similar, but at certain longitudes there exist significant differences. Detailed features of these differences are shown in Figure 12. Positive values (warm colors) represent cases were the reverse current amplitude is larger in the Southern Hemisphere. This is quite obviously the case in the Atlantic region.

For investigating the tidal properties of the hemispheric differences we use the same approach as described above and numerical results are listed in Table 2. Our analysis reveals a dominance of a wave-1 pattern in all seasons. We find again SPW1 and SW3 as the main tidal components. Interestingly, the phase of SPW1 is shifted by 90° to the west compared to the results above from the sideband amplitudes, and the semidiurnal tide SW3 passes the Greenwich meridian on average 5 h in LT earlier. Both these values infer that largest hemispheric differences occur at longitudes where sideband amplitudes show the steepest longitudinal gradients.

As mentioned in section 4.1, hemispheric differences are expected to be caused by meridional winds. Our analysis suggests southward winds centered around −40° longitude and northward winds mainly around 180° longitude. It may be noted that we do not observe in Figure 12 indications for a switch in meridional wind direction between solstices, as expected from the interhemispheric summer-to-winter winds. For explaining the observed differences in amplitude we may take into account the deflection of the EEJ orientation from due eastward. At −45° longitude the current heads with an angle of 13° toward north, and at 180° longitude it is tilted by 10° toward south (see Figure 11 in Lühr et al. (2004)). The prevailing eastward wind in the *E* region thus causes a meridional component pointing southward with respect to the EEJ around −45° longitude and a northward component around 180° longitude. This notion is consistent with our observations of hemispheric differences. It probably needs further dedicated model studies to verify the suggested effects of EEJ deflection.

In Figure 13 the longitude versus local time distribution of the ratio between sideband amplitude and the main EEJ peak current density is shown. From top to bottom again the different stages of tidal analysis are shown. This quantity exhibits a number of similar longitudinal patterns during the equinox seasons (see left column of frames), but significant differences between the solstices. In particular, in the Western Hemisphere variations are out of phase. The tidal analysis provides a rather mixed picture of the ratio. During most

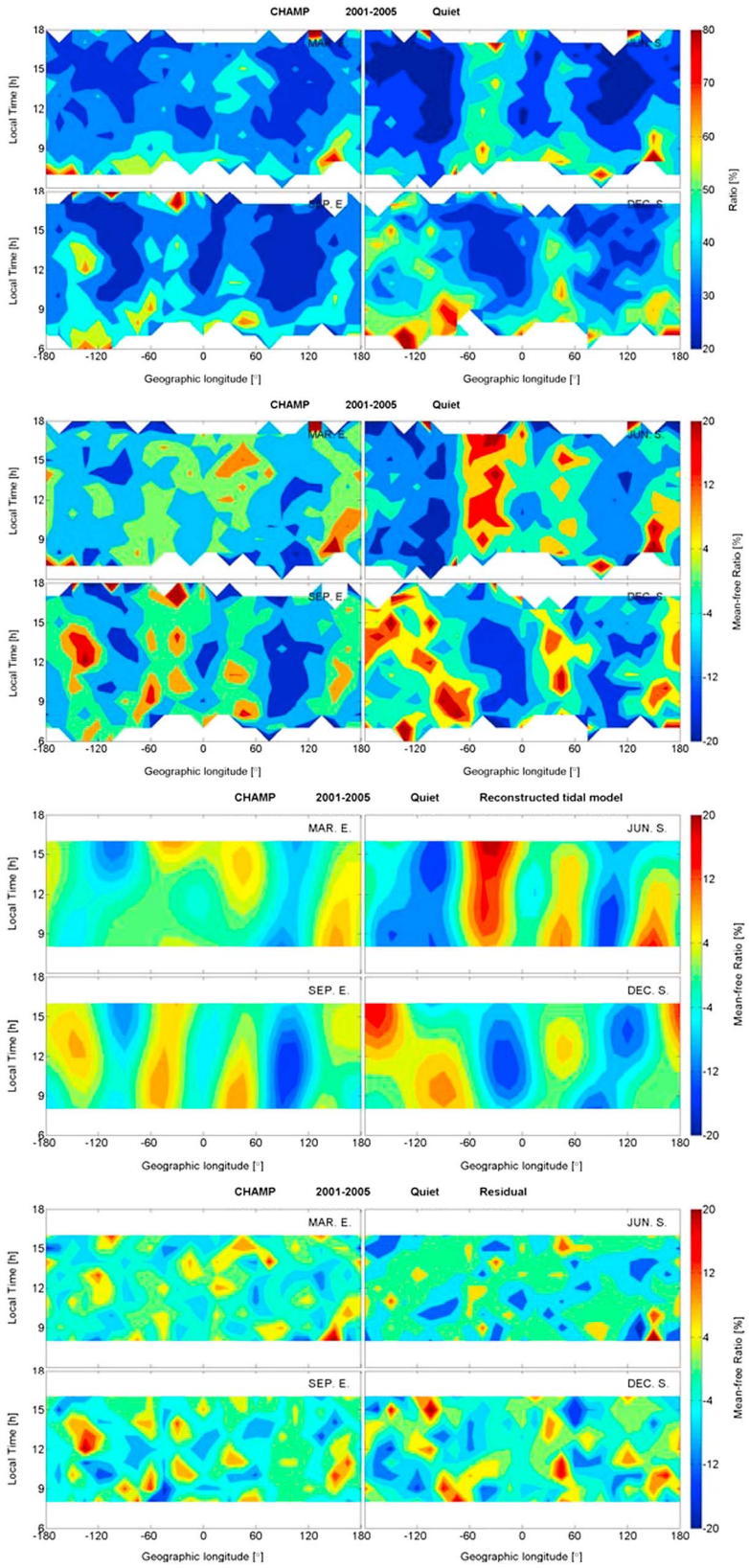

Figure 13. Tidal analysis of the ratio between the sideband and the main EEJ current density. From top to bottom shown are the distribution of the ratio, the mean-free ratios, the longitudinal patterns as reconstructed from the tidal model, and the residuals between observation and model.

Table 3
Same as Table 1 but for the Ratio Between the Sideband and Main EEJ Current Peak Density

	NH & SH ratio							
	Jun		Dec		Mar		Sep	
	Amp. (mA/m)	Phase (Hour)	Amp. (mA/m)	Phase (Hour)	Amp. (mA/m)	Phase (Hour)	Amp. (mA/m)	Phase (Hour)
DE3:	1.80	15.6	1.87	17.3	1.08	9.9	2.66	20.9
DE2:	6.12	23.9	5.32	2.6	4.05	2.4	3.46	0.1
SW3:	5.02	1.1	3.51	7.1	3.19	3.9	1.94	8.6
SW4:	0.82	6.4	4.07	4.3	2.22	4.5	1.62	2.4
TW4:	4.69	0.6	2.50	4.9	1.23	1.9	0.83	0.9
SPW1:	3.34	352.3°	3.37	217.5°	1.54	332.6°	2.25	280.0°
SPW2:	6.66	159.5°	3.72	36.9°	4.16	168.7°	3.68	0.9°
SPW4:	5.91	48.6°	2.57	23.5°	2.63	53.6°	4.11	40.5°

seasons wave-2 and wave-3 patterns are dominating. From Table 3 we can see that DE2 (wave-3) is quite prominent. Largest amplitudes occur during June and December season. This is in line with the importance of that tidal component for the EEJ around solstices, but the derived phases, ranging around midnight, are shifted by about 12 h with respect to the EEJ (e.g., Lühr & Manoj, 2013). Wave-2 signal appears mainly as SPW2. Around December solstice also SW4 is strong, much the same as for the EEJ. For this semidiurnal tide the phase difference is 6 h. Finally, in September the well-known wave-4 patterns are dominating; both SPW4 and DE3 are contributing. All these tidal components and their out-of-phase appearance infer that the longitudinal patterns of the ratio are dominated by the tidal modulation of the main EEJ current and reveal little additional information about the sidebands.

Finally, we investigated the behavior of the latitude where the reverse current density peaks. Figure 14 shows the distribution of that quantity in local time versus longitude frames. In the top panels we can see that larger peak latitudes are confined to morning and evening hours. Around noon the sidebands generally move closer to the equator. In the second group of frames, displaying mean-free quantities after removal of longitudinal averages, certain tidal components can already be recognized. Our analysis reveals that wave-1 patterns are dominating in all seasons. Most prominent is the semidiurnal SW3 tide (see Table 4). Around June solstice also a wave-3 appears that can be related to DE2. During the December season SW4 makes important contributions to wave-2. The importance of both these tidal components during respective seasons is known from the tidal spectrum of the EEJ (e.g., Lühr & Manoj, 2013).

It is interesting to note that we also found for the modulation of the sideband amplitudes (see Figure 11) dominating wave-1 features. In both cases SW3 plays a prominent role. Furthermore, the phases of SW3 in sideband amplitude and location both vary around 8–10 LT (see Tables 1 and 4). This means that larger amplitudes appear at locations closer to the equator (note that the reverse currents come with a negative sign). This is not a strict relation; also, other effects seem to influence the sideband amplitudes, but we can estimate a certain ratio. By comparing the tidal analyses of the sideband amplitudes and peak latitudes, we reveal from the wave-1 components in these two analyses that an equatorward shift of the peak by 1° in latitude increases the reverse current by about 10 mA/m.

Our results are consistent with the predictions of, for example, Reddy and Devasia (1981) who modeled the effects of different zonal wind vertical profiles on the latitudinal profiles of reverse currents. For large positive zonal wind shear in the *E* layer they obtain enhanced reverse currents that move closer to the equator and make the main EEJ current channel narrower. We may thus conclude that the zonal wind shear near the equator is modulated by an effect that exhibits semidiurnal, SW3, features. This inference should of course be verified by direct wind observations.

5. Summary

We have presented a comprehensive analysis of the reverse current EEJ sidebands. They are found to be a rather common feature of the equatorial electrojet system. These westward currents peaking about 5° in latitude on both sides off the magnetic equator exhibit current densities of about one third of the main EEJ

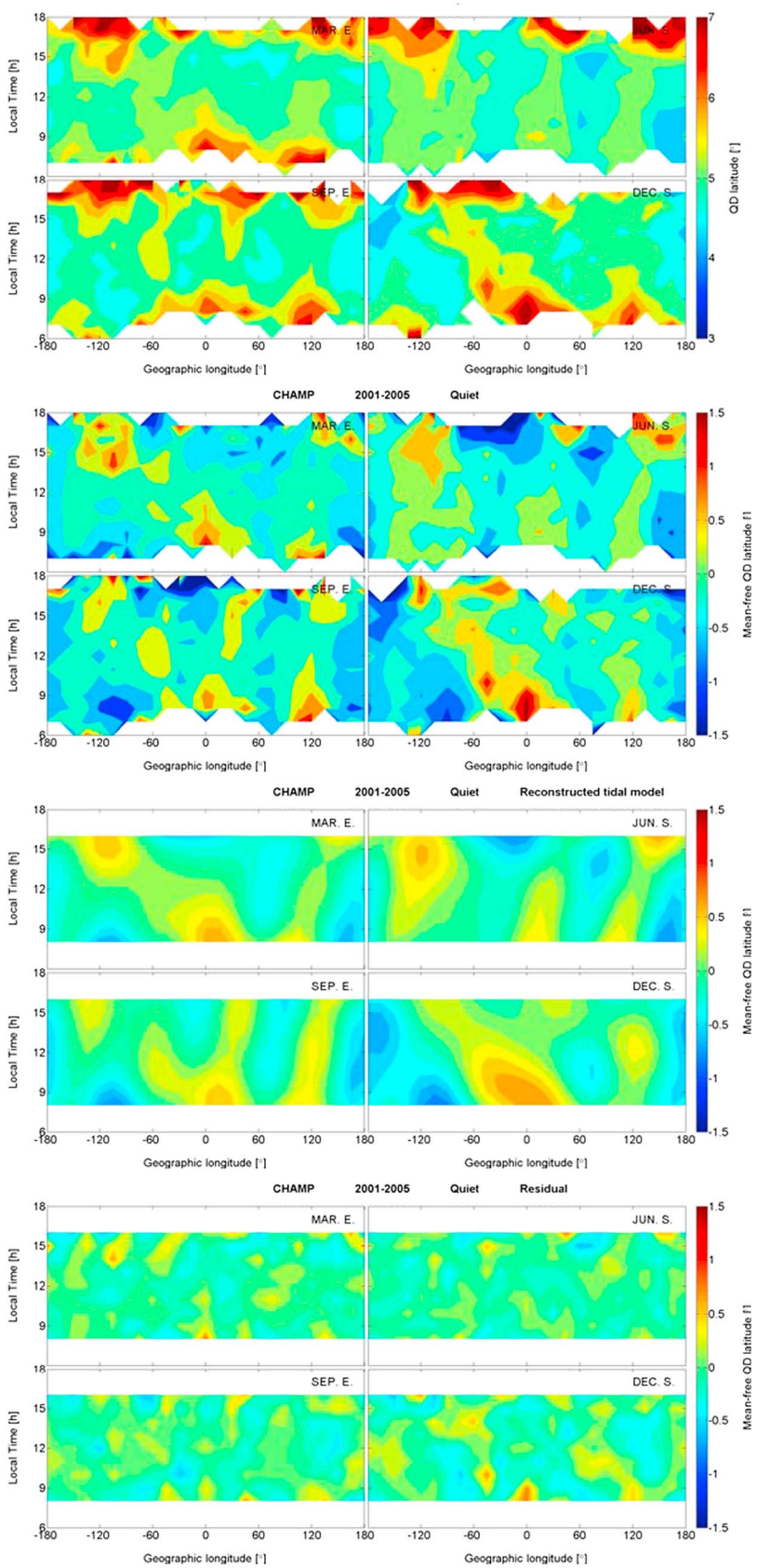

Figure 14. Tidal analysis of the EEJ sideband peak locations. The representation of the signals is the same as in Figure 13.

Table 4
Same as Table 1 but for the QD Latitude of the Sideband Peak Current Location

	NH and SH position							
	Jun		Dec		Mar		Sep	
	Amp. (mA/m)	Phase (Hour)	Amp. (mA/m)	Phase (Hour)	Amp. (mA/m)	Phase (Hour)	Amp. (mA/m)	Phase (Hour)
DE3:	0.23	2.2	0.10	23.1	0.18	1.0	0.17	3.3
DE2:	0.24	10.4	0.15	11.3	0.17	11.6	0.15	10.9
SW3:	0.39	9.0	0.27	10.7	0.51	9.9	0.33	10.5
SW4:	0.01	0.5	0.24	8.2	0.11	8.4	0.12	7.2
TW4:	0.23	5.5	0.20	7.6	0.27	22.5	0.18	7.4
SPW1:	0.08	139.9°	0.23	22.9°	0.10	89.6°	0.13	74.2°
SPW2:	0.13	62.7°	0.10	146.7°	0.002	88.5°	0.02	169.3°
SPW4:	0.09	89.4°	0.07	22.3°	0.12	3.6°	0.09	38.7°

eastward current. Vertical shear of the zonal wind in the upper *E* region has been reported as main driver for the reverse currents at the flanks of the EEJ. A number of average features of the sidebands could be deduced from 5 years of CHAMP magnetic field measurements:

1. The ionospheric conductivity influences the reverse current density. This can be deduced from the diurnal variation of the amplitude and from the dependence on EUV solar flux level. It is interesting to note that the relative variation of the sideband amplitude over a day is less than that of the EEJ, but their dependence on solar flux is stronger.
2. The sideband amplitudes show a certain dependence on longitude. Largest current densities are found over the South Atlantic (~60°W) and Central Pacific (~180°E) and smallest amplitudes close to the Indian sector. Overall, the amplitudes are largest during the December season and smallest around June solstice.
3. The behaviors of the reverse currents on the two sides of the EEJ are quite similar, but there exist significant differences in certain places. Southward wind components enhance westward currents on the south side, and northward winds strengthen reverse currents in the north. Our observations of hemispheric asymmetry imply southward winds over the South Atlantic and northward over the Central Pacific. The seasonal behavior of the hemispheric difference suggests that the prevailing zonal wind in connection with the inclination of the magnetic equator causes the meridional wind effects at the expected longitude sectors.
4. Peaks in reverse current density appear preferably at 5° in latitude off the magnetic equator. Certain variations, however, can be observed. During morning and evening hours peaks occur at larger latitudes (~7°). Around noon they are found mainly around 5° and lower. Our analysis reveals that larger current densities are preferably found at lower latitudes. A shift of 1° toward lower latitude corresponds to about an increase of 10 mA/m in current density.
5. The tidal analysis of the sideband features reveals primarily wave number 1 longitudinal patterns. Main contributions come from the nonmigrating tidal components SW3 (semidiurnal westward propagating) and the stationary SPW1. They probably reflect the interaction of the magnetic equator longitudinal variation with the seasonal and longitudinal variations of the zonal wind. Smallest current densities are observed in the Indian sector (~60°E) where the troughs of the SW3 and SPW1 meet around 12 LT.

The study of the reverse current EEJ sidebands could only make indirect inferences on the properties of the zonal wind. Direct observations of the wind would be desirable for a more reliable modeling of all the electrojet current drivers.

Acknowledgments
The CHAMP mission was sponsored by the Space Agency of the German Aerospace Center (DLR) through funds of the Federal Ministry of Economics and Technology. The CHAMP magnetic field data are available at ftp://magftp.gfz-potsdam.de/CHAMP/L3_DATA. The solar radio flux *F10.7* data can be found at http://omniweb.gsfc.nasa.gov/form/dx1.html. The work of Yun-Liang Zhou is supported by the National Nature Science Foundation of China (41274194 and 41431073).

References

Agu, C. E., & Onwumechili, C. A. (1981). Comparison of the POGO and ground measurements of the magnetic field of the equatorial electrojet. *Journal of Atmospheric and Terrestrial Physics*, *43*(8), 801–807. https://doi.org/10.1016/0021-9169(81)90057-X

Alken, P., & Maus, S. (2007). Spatio-temporal characterization of the equatorial electrojet from CHAMP, Ørsted, and SAC-C satellite measurements. *Journal of Geophysical Research*, *112*, A09305. https://doi.org/10.1029/2007JA012524

Alken, P., Maus, S., Chulliat, A., Vigneron, P., Sirol, O., & Hulot, G. (2015). Swarm equatorial electric field chain: First results. *Geophysical Research Letters*, *42*, 673–680. https://doi.org/10.1002/2014GL062658.

Alken, P., Maus, S., Emmert, J., & Drob, D. P. (2008). Improved horizontal wind model HWM07 enables estimation of equatorial ionospheric electric fields from satellite magnetic measurements. *Geophysical Research Letters*, *35*, L11105. https://doi.org/10.1029/2008GL033580

Alken, P., Maus, S., Vigneron, P., Sirol, O., & Hulot, G. (2013). Swarm SCARF equatorial electric field inversion chain. *Earth, Planets and Space*, *65*(11), 1309–1317. https://doi.org/10.5047/eps.2013.09.008

Anandarao, B. G., & Raghavarao, R. (1979). Effects of vertical shears in the zonal winds on the electrojet. *Space Research*, *19*, 283–286. https://doi.org/10.1016/B978-0-08-023417-5.50050-8

Anandarao, B. G., & Raghavarao, R. (1987). Structural changes of in currents and fields of the equatorial electrojet due to zonal and meridional winds. *Journal of Geophysical Research*, *92*(A3), 2514–2526. https://doi.org/10.1029/JA092iA03p02514

Cain, J. C., & Sweeney, R. E. (1972). *POGO observations of the equatorial electrojet*, *Publication X-645-72-299*. Goddard Space Flight Center, Greenbelt, Maryland.

Cain, J., & Sweeney, R. (1973). The POGO data. *Journal of Atmospheric and Terrestrial Physics*, *35*(6), 1231–1247. https://doi.org/10.1016/0021-9169(73)90021-4

Chapman, S. (1951). The equatorial electrojets detected from the abnormal electric currents distribution over Huancayo, Peru and elsewhere. *Archives for Meteorology, Geophysics, and Bioclimatology. Serie A, Meteorology and Geophysics*, *4*(1), 368–390. https://doi.org/10.1007/BF02246814

Cowling, T. (1933). The electrical conductivity of an ionized gas in the presence of a magnetic field. *Monthly Notices of the Royal Astronomical Society*, *93*, 90–98.

Egedal, J. (1947). The magnetic diurnal variation of the horizontal force near the magnetic equator. *Terrestrial Magnetism and Atmospheric Electricity*, *52*(4), 449–451. https://doi.org/10.1029/TE052i004p00449

Fambitakoye, O., & Mayaud, P. N. (1976). Equatorial electrojet and regular daily variation S_R—I. A determination of the equatorial electrojet parameters. *Journal of Atmospheric and Terrestrial Physics*, *38*(1), 1–17. https://doi.org/10.1016/0021-9169(76)90188-4

Fambitakoye, O., Mayaud, P. N., & Richmond, A. D. (1976). Equatorial electrojet and regular daily variation S_R—III. Comparison of observations with a physical model. *Journal of Atmospheric and Terrestrial Physics*, *38*(2), 113–121. https://doi.org/10.1016/0021-9169(76)90118-5

Finlay, C. C., Olsen, N., Kotsiaros, S., Gillet, N., & Toffner-Clausen, L. (2016). Recent geomagnetic secular variation from Swarm and ground observatories as estimated in the CHAOS-6 geomagnetic field model. *Earth, Planets and Space*, *68*(1), 112. https://doi.org/10.1186/s40623-016-0486-1.

Forbes, J. M. (1981). The equatorial electrojet. *Reviews of Geophysics*, *19*(3), 469–504. https://doi.org/10.1029/RG019i003p00469

Hagan, M. E., & Forbes, J. M. (2002). Migrating and nonmigrating diurnal tides in the middle and upper atmosphere excited by tropospheric latent heat release. *Journal of Geophysical Research*, *107*(D24), 4754. https://doi.org/10.1029/2001JD001236

Hesse, D. (1982). An investigation of the equatorial electrojet by means of ground-based magnetic measurements in Brazil. *Annals of Geophysics*, *38*, 315–320.

Ivers, D., Stening, R., Turner, J., & Winch, D. (2003). Equatorial electrojet from Ørsted scalar magnetic field observations. *Journal of Geophysical Research*, *108*(A2), 1061. https://doi.org/10.1029/2002JA009310

Jadhav, G., Rajaram, M., & Rajaram, R. (2002). A detailed study of equatorial electrojet phenomenon using Ørsted satellite observations. *Journal of Geophysical Research*, *107*(A8), 1175. https://doi.org/10.1029/2001JA000183

Köhnlein, W. A. (1986). A model of the electron and ion temperatures in the ionosphere. *Planetary and Space Science*, *34*(7), 609–630. https://doi.org/10.1016/0032-0633(86)90039-5

Langel, R. A., Purucker, M., & Rajaram, M. (1993). The equatorial electrojet and associated currents as seen in Magsat data. *Journal of Atmospheric and Terrestrial Physics*, *55*(9), 1233–1269. https://doi.org/10.1016/0021-9169(93)90050-9

Lühr, H., & Manoj, C. (2013). The complete spectrum of the equatorial electrojet related to solar tides: CHAMP observations. *Annals of Geophysics*, *31*(8), 1315–1331. https://doi.org/10.5194/angeo-31-1315-2013

Lühr, H., & Maus, S. (2006). Direct observation of the F region dynamo currents and the spatial structure of the EEJ by CHAMP. *Geophysical Research Letters*, *33*, L24102. https://doi.org/10.1029/2006GL028374

Lühr, H., & Maus, S. (2010). Solar cycle dependence of quiet-time magnetospheric currents and a model of their near-Earth magnetic fields. *Earth, Planets and Space*, *62*(10), 843–848. https://doi.org/10.5047/eps.2010.07.012

Lühr, H., Maus, S., & Rother, M. (2004). Noon-time equatorial electrojet: Its spatial features as determined by the CHAMP satellite. *Journal of Geophysical Research*, *109*, A01306. https://doi.org/10.1029/2002JA009656

Lühr, H., Rother, M., Maus, S., Mai, W., & Cooke, D. (2003). The diamagnetic effect of the equatorial Appleton anomaly: Its characteristics and impact on geomagnetic field modeling. *Geophysical Research Letters*, *30*(17), 1906. https://doi.org/10.1029/2003GL017407

Maus, S., Alken, P., & Lühr, H. (2007). Electric fields and zonal winds in the equatorial ionosphere inferred from CHAMP satellite magnetic measurements. *Geophysical Research Letters*, *34*, L23102. https://doi.org/10.1029/2007GL030859

Maus, S., Yin, F., Lühr, H., Manoj, C., Rother, M., Rauberg, J., et al. (2008). Resolution of direction of oceanic magnetic lineations by the sixth-generation lithospheric magnetic field model from CHAMP satellite magnetic measurements. *Geochemistry, Geophysics, Geosystems*, *9*, Q07021. https://doi.org/10.1029/2008GC001949

Oberheide, J., Wu, Q., Killeen, T. L., Hagan, M. E., & Roble, R. G. (2006). Diurnal nonmigrating tides from TIMED Doppler Interferometer wind data: Monthly climatologies and seasonal variations. *Journal of Geophysical Research*, *111*, A10S03. https://doi.org/10.1029/2005JA011491

Onwumechili, C. A. (1992). On the return current of the equatorial electrojet. *Advances in Space Research*, *12*(6), 33–43. https://doi.org/10.1016/0273-1177(92)90037-X

Onwumechili, C. A. (1997). *The equatorial electrojet*. Newark, NJ: Gordon and Breach.

Onwumechili, C., & Agu, C. (1980). General features of the magnetic field of the equatorial electrojet measured by the POGO satellites. *Planetary and Space Science*, *28*(12), 1125–1130. https://doi.org/10.1016/0032-0633(80)90071-9

Reddy, C. A., & Devasia, C. V. (1981). Height and latitude structures of electric fields and currents due to local east-west winds in the equatorial electrojet. *Journal of Geophysical Research*, *86*(A7), 5751–5767. https://doi.org/10.1029/JA086iA07p05751

Reigber, C., Lühr, H., & Schwintzer, P. (2002). CHAMP mission status. *Advances in Space Research*, *30*(2), 129–134. https://doi.org/10.1016/S0273-1177(02)00276-4

Richmond, A. D. (1973). Equatorial elctrojet—I. Development of a model including winds and instabilities. *Journal of Atmospheric and Terrestrial Physics*, *35*, 1083.

Richmond, A. D. (1995). Ionospheric electrodynamics using magnetic apex coordinates. *Journal of Geomagnetism and Geoelectricity*, *47*(2), 191–212. https://doi.org/10.5636/jgg.47.191

Thomas, N., Vichare, G., & Sinha, A. K. (2017). Characteristics of equatorial electrojet derived from Swarm satellites. *Advances in Space Research*, *59*(6), 1526–1538. https://doi.org/10.1016/j.asr.2016.12.019

Zhou, Y.-L., Lühr, H., Alken, P., & Xiong, C. (2016). New perspectives on equatorial electrojet tidal characteristics derived from the Swarm constellation. *Journal of Geophysical Research: Space Physics*, *121*, 7226–7237. https://doi.org/10.1002/2016JA022713